IMMUNOLOGY

Structural basis for flagellin-induced NAIP5 activation

Bhaskar Paidimuddala, Jianhao Cao, Liman Zhang*

The NAIP (NLR family apoptosis inhibitory protein)/NLRC4 (NLR family CARD containing protein 4) inflammasome senses Gram-negative bacterial ligand. In the ligand-bound state, the winged helix domain of NAIP forms a steric clash with NLRC4 to open it up. However, how ligand binding activates NAIP is less clear. Here, we investigated the dynamics of the ligand-binding region of inactive NAIP5 and solved the cryo-EM structure of NAIP5 in complex with its specific ligand, FliC from flagellin, at 2.9-Å resolution. The structure revealed a "trap and lock" mechanism in FliC recognition, whereby FliC-$D0_C$ is first trapped by the hydrophobic pocket of NAIP5, then locked in the binding site by ID (insertion domain) and C-terminal tail of NAIP5. The FliC-$D0_N$ domain further inserts into ID to stabilize the complex. According to this mechanism, FliC triggers the conformational change of NAIP5 by bringing multiple flexible domains together.

INTRODUCTION

The nucleotide-binding domain (NBD), leucine-rich repeat (LRR) domain containing protein family (NLR family) apoptosis inhibitory proteins (NAIPs) constitute a family of cytosolic receptors that mediate host defense against Gram-negative bacteria (*1*). There are multiple NAIP proteins in mice, each of which senses different bacterial ligands. For example, NAIP5 and NAIP6 are activated by flagellin, whereas NAIP2 and NAIP1 are activated by components of bacterial type III secretion system, the inner rod protein, and needle protein, respectively (*2*, *3*). The human genome only encodes one NAIP, which seems to be activated by all three ligands (*4*–*6*). Upon activation, NAIPs recruit and activate the NLR family caspase activation and recruitment domain (CARD) containing protein 4 (NLRC4). Structurally, both NAIP and NLRC4 contain the NBD, helical domain 1 (HD1), winged helix domain (WHD), HD2, and LRR domains. However, their N-terminal effector domains are different. NAIP has three baculovirus IAP repeat (BIR) domains, while NLRC4 has a CARD. Upon activation, NAIP recruits inactive NLRC4 and triggers its conformational change from the inactive state to the active state. Active NLRC4 further oligomerizes and nucleates the filamentation of caspase-1 (*7*–*9*), which eventually leads to the proteolytic activation of interleukin-1β (IL-1β), IL-18, and Gasdermin D (GSDMD), cause pyroptotic cell death (*10*–*12*).

NAIP and NLRC4 have highly similar active structures in their open conformation and form the NAIP/NLRC4 inflammasome complex (*13*, *14*), but they must adopt a stable inactive conformation in resting cells to prevent autoinflammation. NLRC4 achieves this with an autoinhibited conformation that prevents it from oligomerizing. In a recent report, we presented the structure of inactive NAIP in a wide-open conformation (*15*). The distinct inactive conformations of NAIP and NLRC4 suggest that these two proteins should have different activation mechanisms, which leads to the question of how ligand binding induces the activation of NAIP. Previously, two cryo–electron microscopy (cryo-EM) structures containing NAIP5 bound to flagellin have been solved (*13*, *14*), but the electron density in the ligand-binding region was insufficient to support unambiguous model building and led to controversy in the interpretation of ligand-NAIP interaction (*16*).

To understand how ligand binding activates NAIP, we characterized the dynamics of the ligand-binding region of inactive NAIP5 and determined the high-resolution cryo-EM structure of NAIP5 in complex with FliC, the flagellin from *Salmonella typhimurium*, at 2.9-Å resolution. The resulting cryo-EM map allowed us to build atomic models around the ligand-binding region with high confidence. By comparing the structures of unliganded and liganded NAIP5, we have provided molecular insights into how NAIP is activated by ligand binding.

RESULTS

Flexibility of the C-terminal regions in unliganded NAIP5

We previously reported the cryo-EM structure of unliganded NAIP5 in a wide-open conformation (*15*). Unfortunately, despite achieving an overall resolution of 3.4 Å, the density of the HD2-LRR region was absent in the unliganded NAIP5 structure. Here, we conducted further investigations to comprehensively understand the nature of this missing density. Using multi-body refinement in Relion (*17*), we characterized the dynamics of the HD2-LRR regions, and the result demonstrated that the missing regions in the HD2-LRR undergo approximately 30° movement (Fig. 1A and movie S1). Considering that the dynamic regions in HD2-LRR primarily participate in ligand binding, we suggest that their flexibility is functionally important to ligand recognition.

We then attempted to analyze how ligand binding stabilizes the HD2-LRR regions by comparing our unliganded NAIP5 with two previous complexes of ligand/NAIP5/NLRC4 [referred to as Protein Data Bank identifiers (PDB IDs) 6B5B (*13*) and 5YUD (*14*) hereafter]. Unfortunately, the resolutions of ligand-binding regions in both structures are insufficient for unambiguous model building. Consequently, the interpretations of the ligand-NAIP5 interaction in the two structures differ markedly. Specifically, in the case of 5YUD, the flagellin was traced in a manner that positions the loop that connects $D0_N$ and $D0_C$ between HD2 and LRR, resulting in a direct binding to NAIP5. Conversely, $D0_N$ does not participate in the binding and remained unmodeled. However, 6B5B puts $D0_N$ to a helix at the surface of the map between N-terminal domain (NTD) and LRR of NAIP5. The same helix was traced by 5YUD

Department of Chemical Physiology and Biochemistry, Oregon Health and Science University, Portland, OR 97239, USA.
*Corresponding author. Email: zhanglim@ohsu.edu

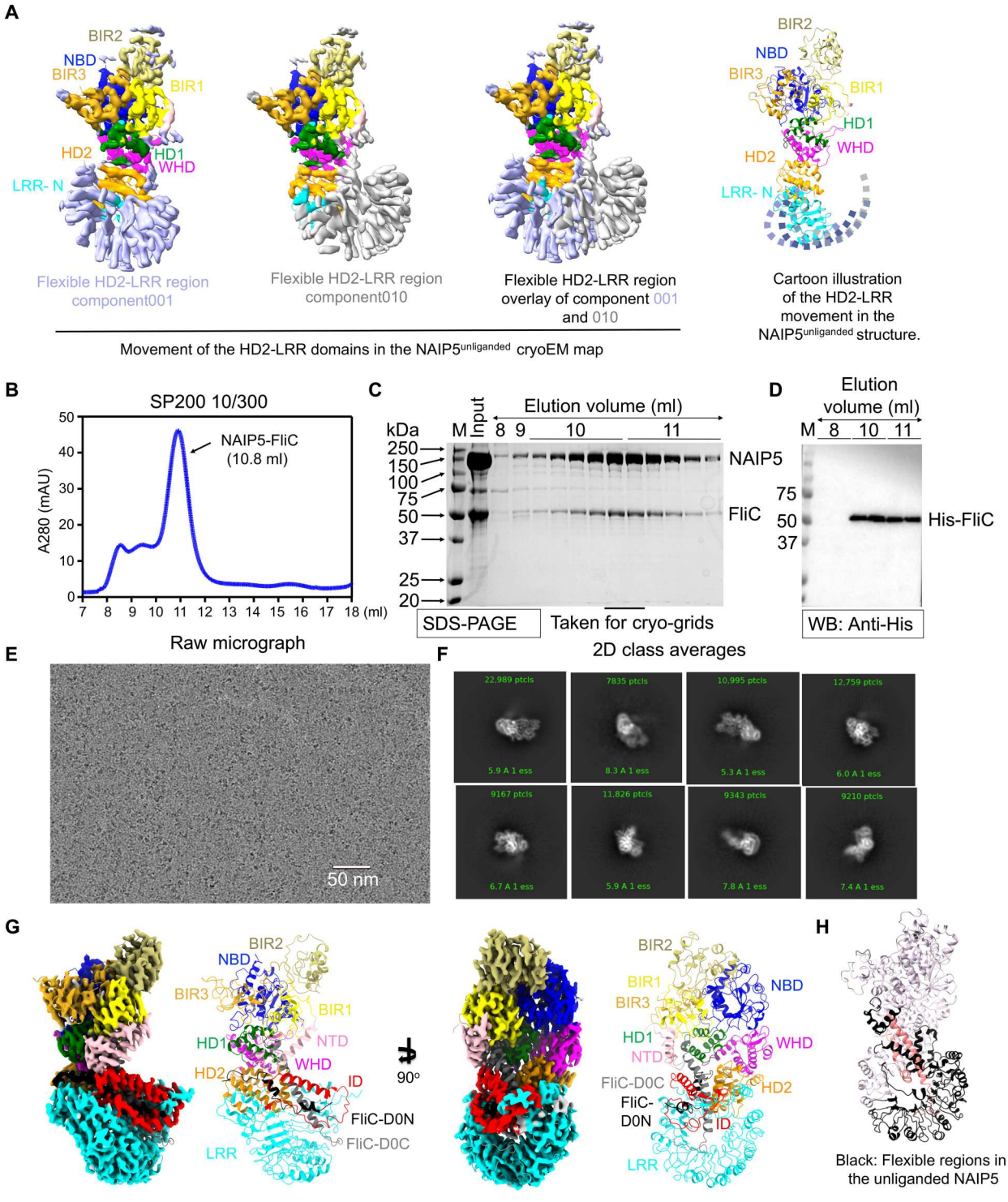

Fig. 1. Dynamics of unliganded NAIP5, biochemical purification, and cryo-EM structure of the NAIP5/FliC complex. (**A**) Multi-body refinement of unliganded NAIP5 in Relion. From Relion multi-body refinement, we obtained 10 maps representing different conformations. Here, we only showed the 1st map (blue) and the 10th map (gray). The blue and gray region includes a part of HD2 and the entire LRR domains. (**B**) SEC profile of the NAIP5/FliC complex. (**C**) SDS-PAGE of fractions in (B). (**D**) Western blot of fractions in (B). (**E**) Representative cryo-EM micrograph and (**F**) 2D class averages showing side view and top/bottom views. (**G**) Cryo-EM map and structure of the NAIP5/FliC complex; individual domains are color-coded. (**H**) The missing densities of unliganded NAIP5 (black) are plotted in the newly resolved NAIP5/FliC structure. FliC is shown in salmon.

as part of the insertion domain (ID); however, the ID remained untraced in the 6B5B model (figs. S1 and S4) (*13*, *14*). To support a mechanistic understanding of how the flexibility in HD2-LRR of NAIP5 accommodates ligand binding and how flagellin binding activates NAIP5, we decided to solve the structure of NAIP5/FliC complex at high resolution.

Biochemical purification and cryo-EM studies of the NAIP5/FliC complex

Given that both 6B5B and 5YUD are solved in complex with NLRC4, which may induce sample heterogeneity and limit the high-resolution structure determination, we decided to take a different approach and reconstitute the complex with only NAIP5 and flagellin. Briefly, we coexpressed full-length NAIP5 with an N-terminal Flag tag and the full-length *S. typhimurium* flagellin, FliC with N-terminal His tag in Expi293F cells. Purification was carried out by anti-Flag affinity purification, followed by size exclusion chromatography (SEC) (Fig. 1B). A large symmetric peak observed at 11 ml in the chromatogram of Superdex 200 showed the presence of NAIP5-FliC complex on SDS–polyacrylamide gel electrophoresis (SDS-PAGE), which was further confirmed by Western blotting (Fig. 1, C and D). The corresponding peak fractions were taken for structure determination. Cryo-EM grids were screened and subjected to data collection under Titan Krios transmission electron microscope equipped with a BioContinuum K3 direct electron detector.

Cryo-EM data processing was performed using cryoSPARC (*18*). Particles extracted from 4616 micrographs were subjected to multiple rounds of two-dimensional (2D) classification before obtaining ab initio maps. Next, the multiple rounds of heterogeneous and homogeneous refinement, followed by local refinement with a default mask, resulted in a high-resolution map of 2.9 Å from the final particle set of 199,022 (Fig. 1, E and G, and fig. S2).

To build the atomic model of active NAIP5, individual BIR domains, NBD, HD1, and WHD from the unliganded NAIP5 (PDB ID 7RAV) and HD2 and LRR from the AlphaFold-predicted structure (AF-Q9R016) (*19*), were fitted into the cryo-EM map (*15*). The side-chain density for most NAIP5 domains was sufficient for manual model building. However, certain regions exhibited lower quality. Specifically, residues 7 to 10 (in NTD), 290 to 295, 328 to 350 (in BIR3), 442 to 452, 524 to 530 (in NBD), 734 to 746 (in WHD), 818 to 820 (in HD2), 1067, 1090 to 1097, 1113 to 1114, 1141 to 1150, 1165 to 1174, 1206 to 1199, 1227 to 1217, 1246 to 1261, 1275 to 1285, and 1332 to 1333 (in LRR domain) were built against less optimal density. For FliC model building, every helix within the D0, D1, D2, and D3 domains were attempted to fit into the non-NAIP5 cryo-EM density, and only the sequence segments comprising residues 495 to 486, 483 to 481, 474 to 470, and 469 to 462 within FliC-$D0_C$, as well as residues 14 to 17 and 20 to 23 within FliC-$D0_N$ could fit into the non-NAIP5 density. Subsequently, manual model building was conducted with these residues as markers. The initial model of NAIP5/FliC complex was then subjected to multiple rounds of refinement using Coot (*20*) and Phenix real-space refinement (fig. S3, A and B, and table S1) (*21*).

The overall shape of our NAIP5/FliC structure is similar to the active NLRC4 (*7*, *8*) and the NAIP5 subunits in both 6B5B and 5YUD (Fig. 1G and fig. S1). To clarify one of the major differences between 6B5B and 5YUD, our structure showed that residues 919 to 982 of NAIP5 form a structured ID and directly contact with FliC. We were also able to confidentially build the ligand-binding region with our high-resolution map, which is different in 6B5B and 5YUD, and mostly flexible in the unliganded NAIP5 structure (Fig. 1H). Our structure reveals molecular details that allowed us to propose the mechanism underlying FliC-induced NAIP5 activation.

Structure of FliC in the NAIP5/FliC complex

Although we used full-length FliC in our sample preparation, the density map only revealed the $D0_N$ helix and $D0_C$ helix, which directly interacted with NAIP5. The remaining part of FliC appeared as a blob in the density map, likely because it is flexibly connected with $D0_N$ and $D0_C$ (Fig. 2A). In monomeric FliC, both $D0_N$ and $D0_C$ have been shown to be disordered (*22*), but they form a coiled-coil structure in the flagella filament (Fig. 2B) (*23*, *24*). Our $D0_N$ and $D0_C$ structures in the NAIP5/FliC complex adopted a helical conformation but showed obvious differences from those in flagella, 6B5B, and 5YUD (Fig. 2B and fig. S4, A and B) (*13*, *14*, *25*). Rather than the coiled-coil structure in flagella, which is essential for the filament formation (*23*, *24*), both $D0_N$ and $D0_C$ in the NAIP5/FliC complex bend in the middle and are separated by NAIP5 ID (Fig. 2A). Considering that only the disordered structure in the monomeric $D0_N$ and $D0_C$ could allow them to separately bind NAIP5, these findings suggest that NAIP5 may only recognize monomeric FliC.

Functionally, it has been shown that $D0_C$ alone could activate the inflammasome to induce IL-1β maturation and cell death, while mutations on the $D0_N$ helix, such as residues 31 to 33 of the *Legionella pneumophila* flagellin, FlaA (corresponding to residues 33 to 35 on FliC) also affect NLRC4 activation (*13*, *14*). However, neither 5YUD nor 6B5B has the interactions of $D0_N$ with NAIP5 properly characterized. In 5YUD, $D0_N$ does not directly interact with NAIP5, while in 6B5B, the $D0_N$ helix was fitted into the density of NAIP5 ID loop (fig. S4B). The residues on NAIP5 that are involved in FliC recognition are assigned differently in 5YUD and 6B5B. Here, our structure showed extensive interactions between $D0_N$ and NAIP5 ID, HD2 domains (Figs. 2A and 3D). We speculate that previous assays to measure the functional readout of the NAIP/NLRC4 inflammasome are less sensitive to define the interactions between NAIP5 and FliC, so we used blue native–PAGE (BN-PAGE) to directly monitor the formation of NAIP5/FliC complex and tested the functional importance of $D0_N$ and $D0_C$ in NAIP5 binding. Compared with full-length FliC, both deletion of N-terminal 27 residues (DN27) or 52 residues (DN52) showed a greatly reduced super-shift band, which indicates that $D0_N$/NAIP5 interaction is important for the complex formation (Fig. 2, C and D). $D0_C$ is indeed critical, as deleting the five residues at the C-terminal end abolished complex formation (Fig. 2, C and D). The NAIP5-Dloop mutation and the nucleating surface mutation that are unable to activate NLRC4 (*15*) could form a normal complex with FliC, which agrees with their proposed functions in triggering NLRC4 conformational change (Fig. 2, C and D).

Interactions between NAIP5 and FliC-$D0_C$

In our structure, NAIP5 and FliC form extensive interactions, with both $D0_N$ (residues 1 to 39) and $D0_C$ (residues 453 to 495) embedded inside NAIP5 (Figs. 1G and 2A). Consistent with 6B5B and 5YUD, the C-terminal residues (487 to 495) of $D0_C$ insert into a hydrophobic pocket formed by the NTD, BIR1, and HD1

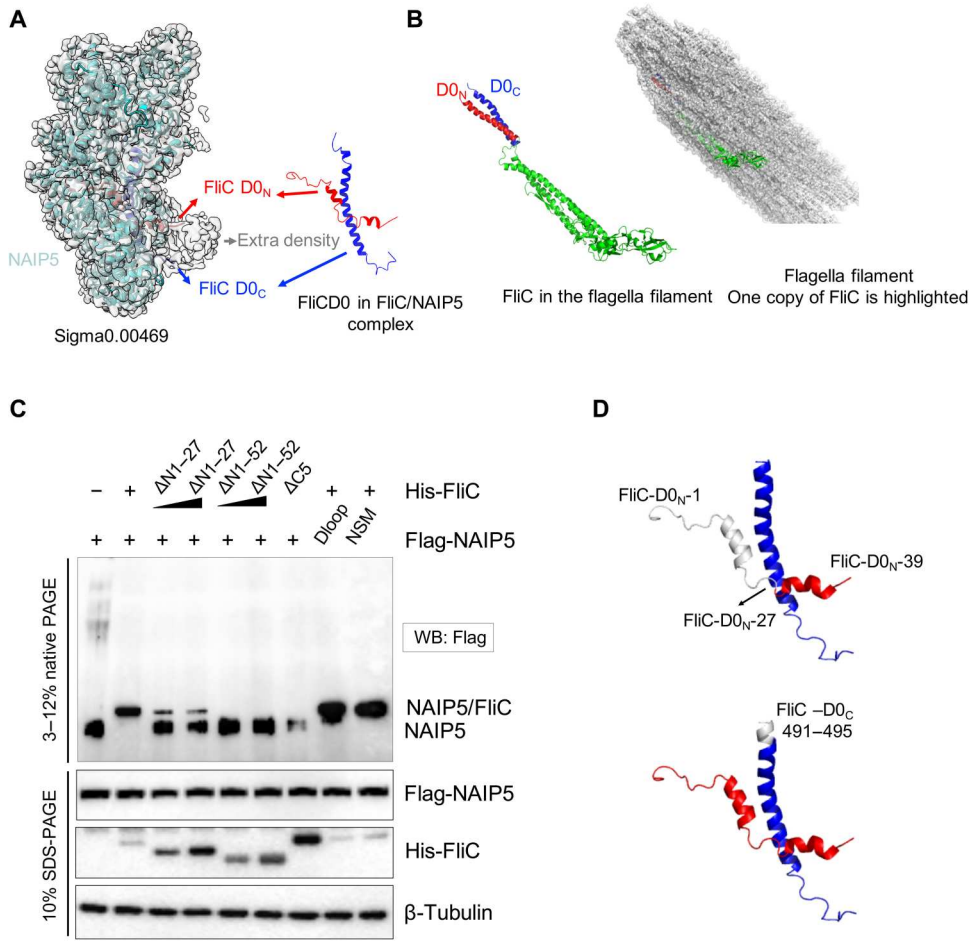

Fig. 2. The FliC subunit in the NAIP5/FliC complex. (**A**) $D0_N$ and $D0_C$ helices of FliC in the cryo-EM map of NAIP5/FliC complex. The extra density that may correspond to part of remaining regions of FliC is labeled. (**B**) $D0_N$ and $D0_C$ in flagella filament. (**C**) Effect of different truncations of FliC on the complex formation. This experiment was repeated three independent times. (**D**) Illustration of the FliC truncations in (C).

domains of NAIP5 (Fig. 3A). This insertion is essential as deletion of the C-terminal five residues abolishes NAIP5/FliC interaction (Figs. 2C and 3D). Notably, the central region of $D0_C$ (470 to 486) is sandwiched by the helices of ID and HD2 domains (Fig. 3B), and the N-terminal end of $D0_C$ (459 to 469) is packed by ID and LRR domains (Fig. 3C and fig. S5).

Except for the C-terminal residues, the importance of the middle part and N-terminal end of $D0_C$ has not been extensively investigated. Thus, we designed mutations to test their ability to form a complex with NAIP5. F844A in HD2 of NAIP5 was used as the positive control as this residue was previously mapped to be important for FliC-induced IL-1β processing (*14*). F844A abolished complex formation on BN-PAGE (Fig. 3D). Regarding FliC mutations, changing residues 470 to 473 into alanine abolished complex formation (Fig. 3D), suggesting that the middle part of FliC is essential for NAIP5 recognition. At the N-terminal end, the removal of residues 453 to 458 has no effect, while the deletion of 453 to 460 is greatly reduced, and the deletion of 453 to 469 completely abolished complex formation (Fig. 3D), suggesting that the packing of residues 459 to 469 by ID and LRR domains are functionally important.

NAIP5-CTT inserts into NAIP5 ID loop to mediate FliC recognition

Having established the importance of residues 459 to 469 of $D0_C$ in FliC/NAIP5 recognition, we went on to analyze the molecular interactions in this region. It is quite interesting that not only $D0_C$ simultaneously binds ID and LRR, the C-terminal tail (CTT; residues 1388 to 1403) of NAIP5 also inserts into the ID loop, with residues 1388 to 1398 forming extensive interactions with the ID and LRR of NAIP5, and the D0 of FliC (Fig. 4A). This is a feature that has not been observed in other NLRs, to the best of our knowledge. Deletion of the CTT residues from 1388 to 1403 abolishes the NAIP5/FliC complex formation. Among them, residues 1388 to 1398 that interact with ID, LRR, and FliC may be more important, as Δ1398–1403 can still bind FliC, although at a reduced level (Fig. 4B and fig. S10). Moreover, NAIP5 with a C-terminal 6×His-, 3×Strep II tag was shown to form the NAIP5/NLRC4 inflammasome (*22*). In our hand, fusion of a C-terminal green fluorescent protein (GFP) tag (25 kDa) does not affect the NAIP5-FliC interaction, but a C-terminal maltose-binding protein (MBP) tag (45 kDa) reduced, and a C-terminal GFP-MBP tag abolished the complex formation (fig. S9). It is hard to definitively determine whether these larger tags block the CTT from inserting into the ID loop. Nonetheless, we speculate that

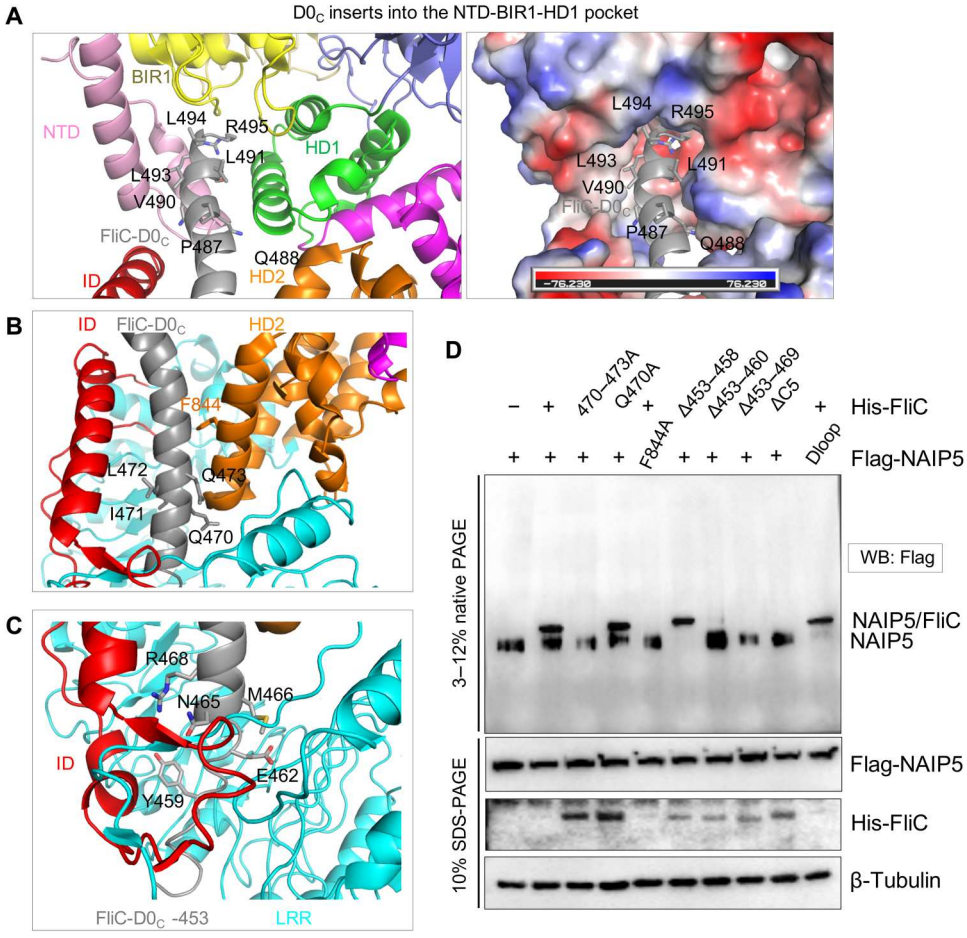

Fig. 3. Interactions between FliC-D0$_C$ and NAIP5. (**A**) The C-terminal residues of D0$_C$ insert into the hydrophobic pocket of NAIP5 formed by NTD, BIR1, and HD1; NAIP5 domains are either color-coded (left) or shown with their surface electrostatic potentials (right). D0$_C$ is in gray. (**B**) The middle part of D0$_C$ (gray) is sandwiched by ID (red) and HD2 (orange). (**C**) The N-terminal part of D0$_C$ (gray) interacts with both ID (red) and LRR (cyan). (**D**) Effect of different D0$_C$ truncations in complex formation. This experiment was repeated three independent times.

even if the CTT does not fully insert into the ID loop, its proximity to the LRR and FliC might enable it to establish contact with them, thereby stabilizing the active conformation of NAIP5. To further narrow down key residues in NAIP5-LRR and CTT, we designed more mutations on NAIP5, including L1393, I1394 to ED (LI-ED); M1361, L1362 to ED (ML-ED); L1365 to A; I1388, I1389, F1390 to DDH (IIF-DDH); and K1392, L1393, I1394 to AGS (KLI-AGS). All the mutations abolished the complex formation and reduced NLRC4 oligomerization (Fig. 4, A and B, and fig. S8).

Next, we mapped the key residues in ID region by separately mutating the ID fragments. Specifically, we changed 936-TYFENL-941 to 6S (6S), 943-PPAIID-947 to 5S (5S), and 954-FEH-956 to 3A (3A). All of them abolished the complex formation and reduced NLRC4 oligomerization (Fig. 4, C and E, and fig. S8). Together, these data suggest that NAIP5/FliC interaction is highly sensitive to the change of sequences in the ID and CTT regions, indicating that an extensive network of ID-D0$_C$-CTT interactions together determines the stability of NAIP5/FliC complex.

Interactions between NAIP5 and FliC-D0$_N$

In our structure, D0$_N$ is inserted into the ID domain and makes contact with both the ID and HD2 domains (Fig. 4D). We have shown before that the DN27 truncation of FliC has a reduced ability to bind to NAIP5 (Fig. 2, C and D). Consistently, the K20 on D0$_N$ forms charge-charge interaction with E975 of NAIP5, and K20E reduced but not abolished FliC/NAIP5 interaction. In comparison, mutations on NAIP5 residues caused a more severe phenotype. For example, both E975R and 970-IIKNY-974 to 5A (5A) mutations that may disrupt D0$_N$-ID interaction abolished complex formation (Fig. 4, D and E).

Proposed mechanism for flagellin-induced NAIP5 activation

With these analyses, we propose a mechanism for flagellin-induced NAIP5 activation. Overall, the recognition of FliC by NAIP5 involves three steps: D0$_C$ trap, CTT-ID lock, and D0$_N$ binding. Because the hydrophobic pocket is the only FliC-binding element that preexists in the inactive NAIP5, the hydrophobic pocket and D0$_C$ interaction is likely the first step in the recognition process. Once the C-terminal residues of D0$_C$ are inserted into the

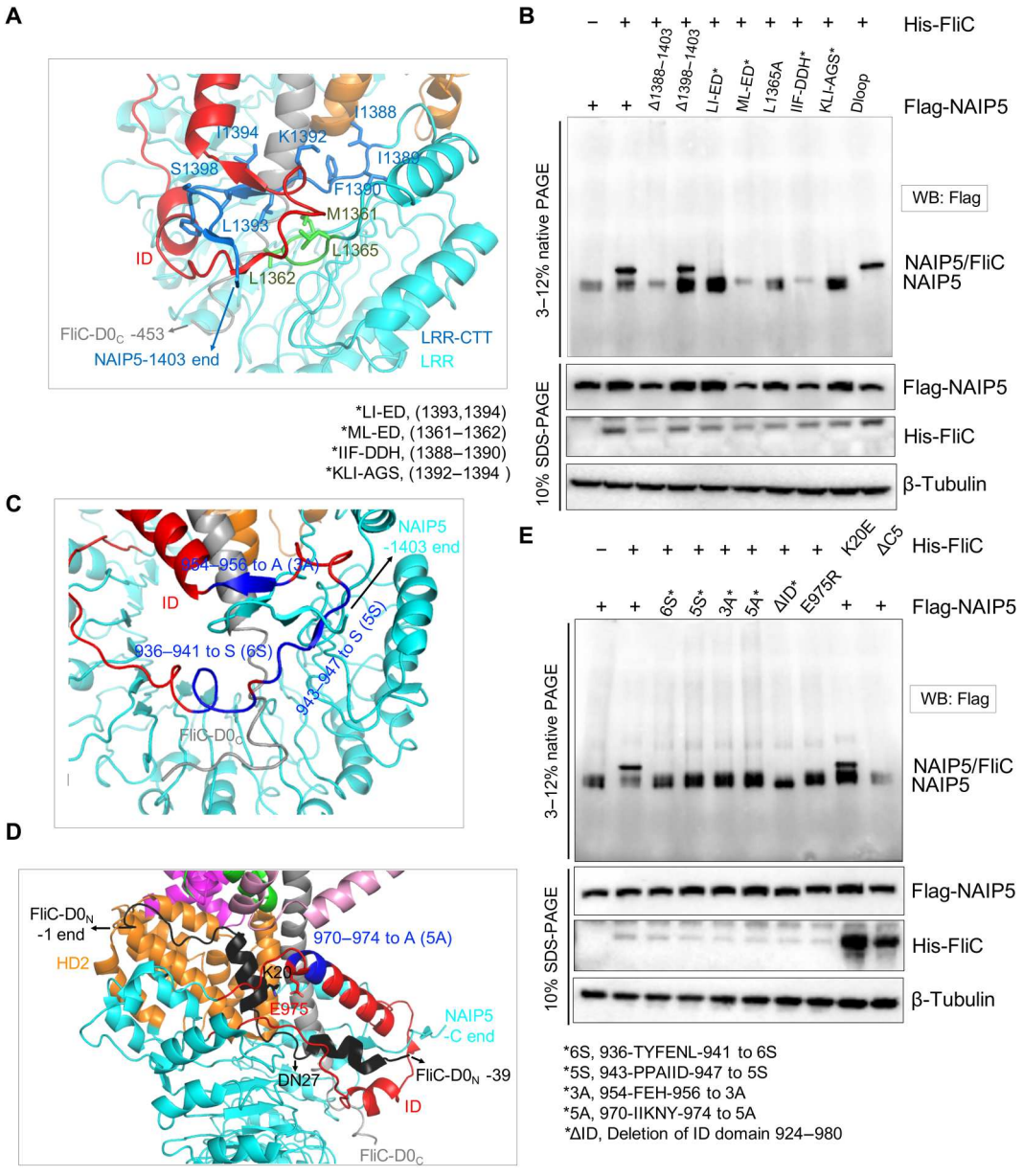

Fig. 4. Interactions in the ID/CTT/D0$_C$ regions. (**A**) The CTT of NAIP5 inserts into the ID loop and forms extensive interactions with the LRR and ID of NAIP5. (**B**) Effects of mutations in the CTT in the complex formation. This experiment was repeated three independent times. (**C**) Residues mapped in the ID loop that are involved in ID/CTT and ID/D0$_C$ interactions. (**D**) D0$_N$ inserts into ID loop and interacts with both ID and HD2. (**E**) Effects of mutations in (C) and (D) in the complex formation. This experiment was repeated three independent times.

hydrophobic pocket, the remaining portion of it forms multiple interactions with the flexible HD2, ID, and LRR domains to create a more rigid structure. This brings the CTT and ID of NAIP5 closer to each other, allowing CTT to insert into the ID loop and lock the D0$_C$ insertion channel, keeping NAIP in the active conformation. Last, D0$_N$ inserts into ID, further stabilizing the complex. Together, the binding of FliC brings the HD2 and LRR domains of NAIP5 to their active positions, indirectly induces the movement of WHD, and forces the 17-18 loop to clash with NLRC4 to open it up (Fig. 4 and movie S2) and eventually initiate the inflammasome signal pathway.

Although the unliganded NAIP5 structure showed a clear adenosine triphosphate (ATP) in the nucleotide-binding pocket (*15*), we did not observe any nucleotide density in the same region of the active NAIP5/FliC complex. Consistently, the conformation of walker A motif (470-**G**ETGS**GKT**-477) seems more flexible in the NAIP5/FliC complex and appears different between these two maps (fig. S5), which suggests that the ATP is hydrolyzed or released in our sample upon ligand binding. However, a previous study has shown that mutating the lysine residue in the walker A motif to arginine (K476R), which reduces ATP binding, does not abolish the activation of NAIP/NLRC4 pathway (*22*). We also tested two walker

A motif mutations, K476A and K476R, and found that neither of them affects the NAIP5/FliC complex formation (fig. S7) or NLRC4 oligomerization (fig. S8). We also showed before that the adenosine triphosphatase (ATPase) activity of NAIP5 is moderate and is not enhanced by FliC (*15*). What is more, a reliable nucleotide density was observed in the NAIP5/FliC complex of 5YUD (*14*), indicating that neither ATP hydrolysis nor release is essential for NAIP5 activation (fig. S5). The differences in ATP binding in our sample and 5YUD could potentially be caused by different expression systems. Together, these findings suggest that the function of nucleotide binding in NAIP may not be as crucial as it is in other NLRs (*26*, *27*).

DISCUSSION

In this study, we focus on the NAIP5-flagellin interactions and proposed a mechanism of FliC-induced NAIP5 activation. Our high-resolution cryo-EM structure of the NAIP5/FliC complex provides detailed insights into the recognition of flagellin by NAIP5 and the subsequent activation of NAIP5. Both the $D0_N$ and $D0_C$ regions of FliC and the ligand-binding regions of NAIP5 exhibit flexibility before their interaction. Structural rearrangements occur in both components during the recognition process, suggesting that the initial FliC recognition may involve weak interactions that are strengthened through structural rearrangement. In addition, the flexibility of the ligand-binding region in unliganded NAIP5 provides the space for initial contact with FliC, enabling it to be trapped in the hydrophobic pocket within the NTD-BIR1-HD1 domains. Furthermore, the insertion of NAIP5-CTT into the ID loop locked $D0_c$ into its binding pocket, and interactions between the ID and $D0_N$ likely contribute to an additional stabilization mechanism. Overall, these interactions directly induce the position of the ID, HD2, and LRR domains at their active conformation, leading to a steric clash between WHD and NLRC4.

It is quite interesting to observe the incorporation of CTT into the ID loop following the binding of the ligand. LRR is commonly used as a ligand-binding domain in Toll-like receptors and NLRs. But this is the first time that the CTT was observed to participate in ligand binding. A functional CTT is essential for stabilizing the NLR proteins and the NAIP/ligand complex. Among the currently solved mammalian NLR structures, NLRP9 also has a CTT and interacts with its LRR (*28*). It will be interesting to see whether the tail appears in other NLRs and whether they are also involved in ligand binding.

MATERIALS AND METHODS

Plasmid constructs

The plasmids pcDNA3.4-Flag-NAIP5, pCMV-6×His-FliC, pBackman-MBP-NLRC4ΔCARD, and pET22b-PA-His were constructed in our previous study (*15*). QuikChange site-directed mutagenesis was performed with either Q5 hot start high-fidelity DNA polymerase-2X master mix (NEB, no. M0494S) or KOD hot start DNA polymerase (MilliporeSigma, no. 71086). pET15b-LFn-FliC plasmid was generated by subcloning FliC sequence from pCMV-6×His-FliC.

Protein expression and purification

Flag-NAIP5 and 6×His-FliC were coexpressed in Expi293F suspension culture by the transient transfection using polyethylenimine reagent (PEI, Polysciences, no. 23966). PEI transfection protocol was the same as described previously (*15*), except the plasmid DNA solution contains 1:3 ratio of NAIP5 and FliC plasmids, respectively. After 72 hours of transfection, cells were collected, washed with ice-cold phosphate-buffered saline (PBS), flash-frozen in liquid nitrogen, and stored at −80°C until use.

On the day of purification, the cell pellet was thawed quickly and lysed in 40 ml per 0.5-liter pellet of Hepes-buffered saline [HBS; 50 mM Hepes (pH 7.5) and 150 mM NaCl] supplemented with 1× protease inhibitor cocktail EDTA free (Abcam, no. ab270055), 10 μg μl^{-1} deoxyribonuclease I (Thermo Fisher Scientific, no. 90083), and 1% Triton X-100. Clarified cell lysate was incubated with anti-flag M2 affinity resin (MilliporeSigma, no. A2220, 0.5 ml, pre-equilibrated in HBS) for 2 hours at constant rotational shaking in a cold room. The protein-bound resin was then collected onto a gravity flow column and washed with 100 ml HBS, and the bound protein was eluted with 5 CV HBS containing 100 μg ml^{-1} 3× Flag peptide (Sigma-Aldrich, no. F4799) and concentrated to 1 ml using Amicon Ultra-4 centrifugal filter unit (molecular weight cutoff, 30 kDa; MilliporeSigma, no. UFC803024). The concentrated protein sample was then subjected to SEC using Superdex 200 Increase 10/300 GL column (Cytiva) in the HBS buffer. SEC fractions were analyzed on Coomassie SDS-PAGE before confirming the fractions containing Flag-NAIP5–6×His-FliC complex. All the purification steps were performed at 4°C.

For in vitro reconstitution, Flag-NAIP5 and 6×His-FliC were expressed separately in Expi293F suspension cultures by using PEI transfection protocol as described earlier (*15*). The purification protocol for Flag-NAIP5 involves flag-tag affinity chromatography followed by SEC as described previously (*15*), except replacing previous buffer with HBS here. The 6×His-FliC purification was done by Ni–nitrilotriacetic acid (NTA) affinity chromatography followed by SEC. Cell lysis and purification buffers were the same as those used for Flag-NAIP5 purification. A similar Ni-NTA purification protocol was used as described earlier (*15*). Ni-NTA–purified FliC was subjected to SEC using Superdex 200 Increase 10/300 GL column (Cytiva) in the HBS buffer. Fractions containing target proteins were analyzed on Coomassie SDS-PAGE. All the purification steps were performed at 4°C.

SEC-purified Flag-NAIP5 and 6×His-FliC were mixed together in 1:3 molar ratio (0.5 ml total volume) and incubated for complex formation at room temperature for 30 min. The incubated sample was then analyzed for complex formation by SEC using Superdex 200 Increase 10/300 GL column (Cytiva) in the HBS buffer followed by Coomassie SDS-PAGE for the collected peak fractions.

NAIP5 truncated versions such as Δ1388–1403 and ΔID were expressed and purified as wild type (WT), as mentioned above. LFn-FliC and protective antigen (PA) were expressed in *Escherichia coli* LOBSTR BL21 cells (Kerafast no. EC1002) and purified by Ni-NTA followed by SEC as described previously (*15*).

Flexibility characterization of the unliganded NAIP5

The dataset previously used for solving the unliganded NAIP5 structure was used in this study to investigate the dynamics of HD2-LRR (*15*). Briefly, particles and cryo-EM map generated by cryoSPARC were exported into Relion format using Pyem (*29*).

The NBD-HD1-WHD domains and HD2-LRR domains were segmented separately from the cryo-EM map using Chimera Segger segementation (*30*, *31*), and the masks for each domain were generated with Relion (*17*, *32*). In Relion's multi-body refinement, the movement relationship between the two domains was defined in body STAR file, setting _rlnBodySigmaAngles to 35 and _rlnBodySigmaOffset to 5. The resulting maps of different confirmations were sharped using deepEMhancer (*33*) and visualized using Chimera's "Volume Series" tool (*30*).

Cryo-EM grid preparation and data collection

To prepare grids for cryo-EM, 4 μl of Flag-NAIP5–6×His-FliC complex (0.9 mg ml^{-1}) was applied to an UltrAuFoil grid (R1.2/1.3 300-mesh, Electron Microscopy Sciences, no. Q350AR13A) that had been glow-discharged for 1 min at 15 mA using a glow discharge cleaning system (PELCO easiGlow, Ted Pella). Vitrification was carried out using Mark IV Vitrobot (Thermo Fisher Scientific) set to 4°C and 100% humidity with 10 s wait and 1.5 s blot times at zero blot force. Grids were screened on either Talos Arctica or Glacios, and the best grids were selected for data collection.

Titan Krios (Thermo Fisher Scientific) equipped with BioQuantum energy filter (Gatan, 20 eV slit width) and K3 Summit direct electron detection camera (Gatan) was used to perform the data collection. The movies were recorded in super-resolution mode with SerialEM (*34*) at a nominal magnification of ×81,000 (calibrated pixel size 0.528 Å). The total dose was set to 50 $e^{-}/Å^2$, with 50 frames per movie and a per frame electron fluence of 1.0 $e^{-}/Å^2$, and defocus range from 1.0 to 2.5 μm.

Cryo-EM data processing and model building

CryoSPARC Live (*18*) was used to evaluate data quality when the data collection was on the fly. A full-fledged data processing was carried out using CryoSPARC (*18*) with a single dataset that constitutes a total of 4616 movies. Movies were subjected to patch motion correction followed by patch CTF estimation. The resulting micrographs were manually curated for optimal CTF fit resolution (7 Å or better) and relative ice thickness, and 2552 micrographs were selected for particle picking. Blob picker tool was used initially to pick the particles, which were subjected to 2D classification to generate the templates for template picker. The resulting stack of 4,486,478 particles was subjected to multiple rounds of 2D classification to remove junk particles, leaving 238,223 particles for the 3D reconstitution. Ab initio reconstitution followed by heterogeneous refinement revealed two classes of NAIP5-FliC volumes and one class of poorly resolved volume. A total of 199,022 particles encompassing the two classes of NAIP5-FliC volumes were combined and subjected to homogeneous refinement, which substantially improved the resolution. Further refinement was carried out by nonuniform refinement followed by local refinement, which eventually resulted in a final map with a gold standard Fourier shell correlation resolution of 2.93 Å. The final map was subjected to postprocessing with DeepEMhancer (*35*) before proceeding for model building.

The atomic model of NAIP5-FliC complex was built using the individual domains from the unliganded NAIP5 (PDB: 7RAV) and NAIP5 AlphaFold model (AF_Q9R016) (*15*, *19*). Individual domains of NAIP5 were initially placed into the density map with ChimeraX (*36*). FliC model was built de novo according to the observed electron densities. Multiple rounds of refinement and building were performed with Phenix real-space refinement and COOT (*20*, *21*). Molecular visualizations were carried out with ChimeraX and PyMOL (*36*, *37*).

NAIP5 and FliC-binding assay

Human embryonic kidney (HEK) 293T cells were cotransfected with Flag-NAIP5 and 6×His-FliC using PEI transfection reagent in a 12-well plate. After 48 hours of transfection, cells were washed with ice-cold PBS before subjected to cell lysis with the buffer containing 1% digitonin, as described previously (*2*). Clarified cell lysates were subjected to 3 to 12% BN-PAGE as per the manufacturer's recommendations (Native PAGE Novex Bis-Tris Gel System, Thermo Fisher Scientific), followed by Western blots against specific antibodies. Antibodies used were as follows: anti-Flag (Sigma-Aldrich, no. F1804), THE His tag antibody (GenScript, no. A00186), anti–β-tubulin (Cell Signaling Technology, no. 86298), and anti-mouse immunoglobulin G, horseradish peroxidase–linked (Cell Signaling Technology, no.7076).

NLRC4 oligomerization assay

Flag-NAIP5 and MBP-NLRC4ΔCARD were cotransfected into HEK293T cells grown in a 12-well plate using PEI transfection reagent. After 24 hours of transfection, purified LFn-FliC and PA proteins each at 30 μg per well were added to allow their translocation into the cells. After another 24 hours of incubation, cells were harvested and clarified lysates were analyzed using 3 to 12% BN-PAGE followed by Western blots against specific antibodies as described previously (*15*).

Thermal shift assay

For determining the stability of NAIP5 truncated versions, the SEC-purified proteins (at 2 μM; 20 μl) were analyzed for their melting curves by adding the SYPRO Orange Protein Gel Stain (Thermo Fisher Scientific, no. S6650) at 1× final concentration, followed by melt curve generation using real-time polymerase chain reaction (PCR) system (Applied Biosystems QuantStudio 7 Flex, 96-well). All the parameters for the generation and analysis of melting curves followed the standard protocol (*35*).

Supplementary Materials

This PDF file includes:
Figs. S1 to S10
Table S1
Legends for movies S1 and S2

Other Supplementary Material for this manuscript includes the following:
Movies S1 and S2

REFERENCES AND NOTES

1. I. Rauch, J. L. Tenthorey, R. D. Nichols, K. Al Moussawi, J. J. Kang, C. Kang, B. I. Kazmierczak, R. E. Vance, NAIP proteins are required for cytosolic detection of specific bacterial ligands in vivo. *J. Exp. Med.* **213**, 657–665 (2016).
2. E. M. Kofoed, R. E. Vance, Innate immune recognition of bacterial ligands by NAIPs determines inflammasome specificity. *Nature* **477**, 592–595 (2011).
3. Y. Zhao, J. Yang, J. Shi, Y. N. Gong, Q. Lu, H. Xu, L. Liu, F. Shao, The NLRC4 inflammasome receptors for bacterial flagellin and type III secretion apparatus. *Nature* **477**, 596–600 (2011).
4. J. Yang, Y. Zhao, J. Shi, F. Shao, Human NAIP and mouse NAIP1 recognize bacterial type III secretion needle protein for inflammasome activation. *Proc. Natl. Acad. Sci. U.S.A.* **110**, 14408–14413 (2013).

5. V. M. Reyes Ruiz, J. Ramirez, N. Naseer, N. M. Palacio, I. J. Siddarthan, B. M. Yan, M. A. Boyer, D. A. Pensinger, J. D. Sauer, S. Shin, Broad detection of bacterial type III secretion system and flagellin proteins by the human NAIP/NLRC4 inflammasome. *Proc. Natl. Acad. Sci. U.S.A.* **114**, 13242–13247 (2017).
6. J. Kortmann, S. W. Brubaker, D. M. Monack, Cutting edge: Inflammasome activation in primary human macrophages is dependent on flagellin. *J. Immunol.* **195**, 815–819 (2015).
7. Z. Hu, Q. Zhou, C. Zhang, S. Fan, W. Cheng, Y. Zhao, F. Shao, H. W. Wang, S. F. Sui, J. Chai, Structural and biochemical basis for induced self-propagation of NLRC4. *Science* **350**, 399–404 (2015).
8. L. Zhang, S. Chen, J. Ruan, J. Wu, A. B. Tong, Q. Yin, Y. Li, L. David, A. Lu, W. L. Wang, C. Marks, Q. Ouyang, X. Zhang, Y. Mao, H. Wu, Cryo-EM structure of the activated NAIP2-NLRC4 inflammasome reveals nucleated polymerization. *Science* **350**, 404–409 (2015).
9. Z. Hu, C. Yan, P. Liu, Z. Huang, R. Ma, C. Zhang, R. Wang, Y. Zhang, F. Martinon, D. Miao, H. Deng, J. Wang, J. Chang, J. Chai, Crystal structure of NLRC4 reveals its autoinhibition mechanism. *Science* **341**, 172–175 (2013).
10. N. Kayagaki, I. B. Stowe, B. L. Lee, K. O'Rourke, K. Anderson, S. Warming, T. Cuellar, B. Haley, M. Roose-Girma, Q. T. Phung, P. S. Liu, J. R. Lill, H. Li, J. Wu, S. Kummerfeld, J. Zhang, W. P. Lee, S. J. Snipas, G. S. Salvesen, L. X. Morris, L. Fitzgerald, Y. Zhang, E. M. Bertram, C. C. Goodnow, V. M. Dixit, Caspase-11 cleaves gasdermin D for non-canonical inflammasome signalling. *Nature* **526**, 666–671 (2015).
11. J. Shi, Y. Zhao, K. Wang, X. Shi, Y. Wang, H. Huang, Y. Zhuang, T. Cai, F. Wang, F. Shao, Cleavage of GSDMD by inflammatory caspases determines pyroptotic cell death. *Nature* **526**, 660–665 (2015).
12. A. Lu, Y. Li, F. I. Schmidt, Q. Yin, S. Chen, T.-M. Fu, A. B. Tong, H. L. Ploegh, Y. Mao, H. Wu, Molecular basis of caspase-1 polymerization and its inhibition by a new capping mechanism. *Nat. Struct. Mol. Biol.* **23**, 416–425 (2016).
13. J. L. Tenthorey, N. Haloupek, J. R. López-Blanco, P. Grob, E. Adamson, E. Hartenian, N. A. Lind, N. M. Bourgeois, P. Chacón, E. Nogales, R. E. Vance, The structural basis of flagellin detection by NAIP5: A strategy to limit pathogen immune evasion. *Science* **358**, 888–893 (2017).
14. X. Yang, Fan Yang, Weiguang Wang, Guangzhong Lin, Zehan Hu, Zhifu Han, Y. Qi, L. Zhang, J. Wang, S.-F. Sui, J. Chai, Structural basis for specific flagellin recognition by the NLR protein NAIP5. *Cell Res.* **28**, 35–47 (2018).
15. B. Paidimuddala, J. Cao, G. Nash, Q. Xie, H. Wu, L. Zhang, Mechanism of NAIP-NLRC4 inflammasome activation revealed by cryo-EM structure of unliganded NAIP5. *Nat. Struct. Mol. Biol.* **30**, 159–166 (2023).
16. L. Zhang, H. Wu, Bad germs are trapped. *Cell Res.* **28**, 141–142 (2018).
17. T. Nakane, S. H. W. Scheres, Multi-body refinement of cryo-EM images in RELION. *Methods Mol. Biol.* **2215**, 145–160 (2021).
18. A. Punjani, J. L. Rubinstein, D. J. Fleet, M. A. Brubaker, CryoSPARC: Algorithms for rapid unsupervised cryo-EM structure determination. *Nat. Methods* **14**, 290–296 (2017).
19. J. Jumper, R. Evans, A. Pritzel, T. Green, M. Figurnov, O. Ronneberger, K. Tunyasuvunakool, R. Bates, A. Žídek, A. Potapenko, A. Bridgland, C. Meyer, S. A. A. Kohl, A. J. Ballard, A. Cowie, B. Romera-Paredes, S. Nikolov, R. Jain, J. Adler, T. Back, S. Petersen, D. Reiman, E. Clancy, M. Zielinski, M. Steinegger, M. Pacholska, T. Berghammer, S. Bodenstein, D. Silver, O. Vinyals, A. W. Senior, K. Kavukcuoglu, P. Kohli, D. Hassabis, Highly accurate protein structure prediction with AlphaFold. *Nature* **596**, 583–589 (2021).
20. P. Emsley, B. Lohkamp, W. G. Scott, K. Cowtan, Features and development of Coot. *Acta. Crystallogr. D Biol. Crystallogr.* **66**, 486–501 (2010).
21. P. V. Afonine, B. K. Poon, R. J. Read, O. V. Sobolev, T. C. Terwilliger, A. Urzhumtsev, P. D. Adams, Real-space refinement in PHENIX for cryo-EM and crystallography. *Acta. Crystallogr. D Struct. Biol.* **74**, 531–544 (2018).
22. E. F. Halff, C. A. Diebolder, M. Versteeg, A. Schouten, T. H. C. Brondijk, E. G. Huizinga, Formation and structure of a NAIP5-NLRC4 inflammasome induced by direct interactions with conserved N- and C-terminal regions of flagellin. *J. Biol. Chem.* **287**, 38460–38472 (2012).
23. S. I. Aizawa, F. Vonderviszt, R. Ishima, K. Akasaka, Termini of salmonella flagellin are disordered and become organized upon polymerization into flagellar filament. *J. Mol. Biol.* **211**, 673–677 (1990).
24. Maki-Yonekura, K. Yonekura, K. Namba, Conformational change of flagellin for polymorphic supercoiling of the flagellar filament. *Nat. Struct. Mol. Biol.* **17**, 417–422 (2010).
25. F. Vonderviszt, S. Kanto, S. Aizawa, K. Namba, Terminal regions of flagellin are disordered in solution. *J. Mol. Biol.* **209**, 127–133 (1989).
26. J. Cao, G. Nash, L. Zhang, Structural mechanisms of inflammasome regulation revealed by cryo-EM studies. *Curr. Opin. Struct. Biol.* **75**, 102390 (2022).
27. J. Wang, W. Song, J. Chai, Structure, biochemical function, and signaling mechanism of plant NLRs. *Mol. Plant* **16**, 75–95 (2023).
28. Y. Kamitsukasa, K. Nakano, K. Murakami, K. Hirata, M. Yamamoto, T. Shimizu, U. Ohto, The structure of NLRP9 reveals a unique C-terminal region with putative regulatory function. *FEBS Lett.* **596**, 876–885 (2022).
29. D. Asarnow, E. Palovcak, Y. Cheng, asarnow/pyem: UCSF pyem v0.5 (v0.5). Zenodo (2019).
30. E. F. Pettersen, T. D. Goddard, C. C. Huang, G. S. Couch, D. M. Greenblatt, E. C. Meng, T. E. Ferrin, UCSF Chimera—A visualization system for exploratory research and analysis. *J. Comput. Chem.* **25**, 1605–1612 (2004).
31. G. D. Pintilie, J. Zhang, T. D. Goddard, W. Chiu, D. C. Gossard, Quantitative analysis of cryo-EM density map segmentation by watershed and scale-space filtering, and fitting of structures by alignment to regions. *J. Struct. Biol.* **170**, 427–438 (2010).
32. S. H. Scheres, RELION: Implementation of a Bayesian approach to cryo-EM structure determination. *J. Struct. Biol.* **180**, 519–530 (2012).
33. R. Sanchez-Garcia, J. Gomez-Blanco, A. Cuervo, J. M. Carazo, C. O. S. Sorzano, J. Vargas, DeepEMhancer: A deep learning solution for cryo-EM volume post-processing. *Commun. Biol.* **4**, 874 (2021).
34. D. Mastronarde, SerialEM: A program for automated tilt series acquisition on tecnai microscopes using prediction of specimen position. *Microsc. Microanal.* **9**, 1182–1183 (2003).
35. K. Huynh, C. L. Partch, Analysis of protein stability and ligand interactions by thermal shift assay. *Curr. Protoc. Protein Sci.* **79**, 28.9.1–28.9.14 (2015).
36. E. F. Pettersen, T. D. Goddard, C. C. Huang, E. C. Meng, G. S. Couch, T. I. Croll, J. H. Morris, T. E. Ferrin, UCSF ChimeraX: Structure visualization for researchers, educators, and developers. *Protein Sci.* **30**, 70–82 (2021).
37. L. Schrödinger, DeLano W, PyMOL (2020); http://pymol.org/pymol.

Acknowledgments: We thank C. Lopez and S. Adamou at the Multiscale Microscopy Core of OHSU and J. Myers, S. Mulligan, C. Yoshioka, and V. Rayaprolu at the Pacific Northwest Center for Cryo-EM (PNCC) for help in cryo–electron microscopy operation. We thank X. Xiao, F. Valiyaveetil, and S. Chatterjee for help with thermal shift assay. **Funding:** A portion of this research was supported by NIH grant U24GM129547 and performed at the PNCC at OHSU and accessed through EMSL (grid.436923.9), a DOE Office of Science User Facility sponsored by the Office of Biological and Environmental Research. This work was supported by National Institutes of Health grant R01AI165580 (L.Z.). We apologize to authors whose work could not be cited because of space limitation. **Author contributions:** B.P., L.Z., and J.C. conceived the study, designed the experiments, and analyzed the data. B.P. reconstituted the protein complex, performed cryo-EM experiments, and refined the structure. B.P. and L.Z. analyzed the structure and designed structure-based mutants. B.P. performed biochemical assays. J.C. analyzed the dynamics of unliganded NAIP5. B.P., L.Z., and J.C. wrote the manuscript. **Competing interests:** The authors declare that they have no competing interests. **Data and materials availability:** All data needed to evaluate the conclusions in the paper are present in the paper and/or the Supplementary Materials. The cryo-EM map of the protein complex was deposited in the Electron Microscopy Data Bank under the accession ID: EMD-29296, and the atomic coordinates were deposited in the PDB under the accession ID: 8FML.

Submitted 28 May 2023
Accepted 6 November 2023
Published 6 December 2023
10.1126/sciadv.adi8539